DOI: 10.1002/((please add manuscript number))
Article type: Communication

Coupling nanostructured CsNiCr Prussian Blue Analogue to resonant microwave fields

Alberto Ghirri, Christian Herrero, Sandra Mazérat, Talal Mallah, Oscar Moze and Marco Affronte*

Dr. A. Ghirri
Istituto Nanoscienze – CNR, via Campi 213/a, 41125 Modena, Italy
E-mail: alberto.ghirri@nano.cnr.it
Dr. C. Herrero, Dr. S. Mazérat, Prof. T. Mallah,
Institut de Chimie Moléculaire et des Matériaux d'Orsay, CNRS, Université Paris Sud, Université Paris Saclay, 91405 Orsay, France
Prof. O. Moze, Prof. M. Affronte
Dipartimento di Fisica, Informatica e Matematica, Università di Modena e Reggio Emilia and Istituto Nanoscienze – CNR, via Campi 213/a, 41125 Modena, Italy

Keywords: (ferromagnetic resonance, coherent spin-photon coupling, magnonics, Prussian Blue Analogues, coordination nanoparticles)

Collective spin excitations in magnetically ordered materials are exploited for advanced applications in magnonics and spintronics. In these contexts, conditions for minimizing dissipative effects are sought in order to obtain long living excitations that can be coherently manipulated. Organic and coordination materials may offer alternative options for their flexibility and low spin-orbit effects. Likewise, ferromagnetic nanostructures provide a versatile platform for hybrid architectures, yet downsizing affects the spin dynamics and needs to be controlled. Here we report a systematic investigation on insulating $CsNiCr(CN)_6$ Prussian blue analogue, including isolated nanoparticles dispersed in polyvinylpyrrolidone polymer, mutually interacting nanoparticles embedded in cetyltrimethylammonium matrix and bulk samples. We performed ferromagnetic resonance spectroscopy in a wide temperature range across the bulk ferromagnetic transition occurring at T_C=90 K. This allows us to

monitor key parameters through different types of nanostructured samples. We found that, below T_C, the Gilbert damping parameter of 10 nm nanoparticles compares well (10^{-3}) with values reported for prototypical yttrium iron garnet $Y_3Fe_5O_{12}$. Strong coupling with the microwave field of a microstrip resonator is then observed for bulk $CsNiCr(CN)_6$ as well as for interacting NPs. These results clarify conditions for the coherent manipulation of collective spin degrees of freedom in nanostructured coordination materials.

In a single domain magnetically ordered material, the fast dynamics of the magnetization is described as precession around an effective magnetic field damped by magnetic viscosity. Under the excitation of electromagnetic (micro)wave, nutation and energy exchange occurs at resonance, as evidenced in ferromagnetic resonance (FMR) experiments. Magnetic materials with low damping are now attracting much interest for their use in spintronics and magnonics since they allow generation and propagation of magnons (i.e. spin excitations of quasistatic magnetization) with low dissipation. For instance, spin pumping at the interface between a ferromagnet and normal metal has been proved as an efficient method to generate a spin current,[1] materials with long living spin waves are used in spin caloritronics [2, 3] whilst controlled interference of spin waves are currently been investigated for non-boolean logic devices operating with low power consumption.[4, 5] In particular conditions, i.e. when the coupling with electromagnetic radiation becomes stronger than damping, coherent dynamics of the magnetization and photons occurs thus allowing the realization of hybrid circuits in which the transfer of magnetic excitations to microwaves takes place with high fidelity[6] and eventually in the quantum regime, i.e. when few excitations are involved.[7]

In these research areas, yttrium iron garnet $Y_3Fe_5O_{12}$ (short, YIG) [8, 9] is considered the reference inorganic (ferri-)magnetically ordered material for its low damping coefficient, yet

its performance critically depends on the size and shape of the specimen. In search of alternative materials to be grown on different substrates and possibly to be scaled up/down in size, high performances, i.e. sharp resonance linewidth, have been recently reported in organic-based ferrimagnetic vanadium tetracyanoethylene thin films.[10] Prussian blue analogues (PBA) are characterized by cyanide coordination ligands and Heisenberg exchange coupling between transition metal spins.[11] FMR spectroscopy has been reported for a few PBA compounds.[12-14] Here, we consider the $CsNi^{II}Cr^{III}(CN)_6$ derivative (CsNiCr in short) which has a face-centered cubic unit cell. Ferromagnetic exchange coupling between the Ni and the Cr sublattices induces magnetic order at Curie temperature T_C(bulk) = 90 K.[11, 15] Isolated CsNiCr nanoparticles (NPs) dispersed in polyvinylpyrrolidone (PVP) organic polymer have been synthesized with a narrow size distribution.[16, 17] Effects of inter-particle coupling were not evident for CsNiCr nanoparticles highly diluted in PVP matrix. Conversely, dispersion in cetyltrimethylammonium (CTA^+) matrix is not effective to magnetically decouple CsNiCr nanoparticles.[18] Indeed, in the latter case, magnetometry and small angle neutron scattering (SANS) experiments evidenced the presence of sizeable inter-particle interactions with magnetic correlation lengths estimated to be (12 ± 4) nm for 8.6 nm NPs and (40 ± 20) nm for 4.8 nm NPs.[19]

We first performed broadband FMR spectroscopy in the 1-26 GHz frequency (ω) range by means of a microstrip transmission line to identify the main features of the absorption spectra. This study was systematically performed on 3 types of samples: bulk, NPs diluted in PVP polymer and NPs embedded in a CTA^+ matrix. Moreover, three (two) sizes of NPs [6, 8 and 10 nm (4.8 and 8.6 nm)] dispersed in PVP (CTA^+) were investigated in order to evaluate size effects on FMR spectra.

Figure 1(a) shows FMR spectra taken on a bulk sample of CsNiCr. A faint FMR absorption dip is visible above T_C (110 K), which becomes well pronounced at the Curie temperature (T_C = 90 K). For lower temperatures (T < 60 K) and for each frequency of excitation, the absorption dip gets smaller and the resonance line broadens. The position of the FMR line linearly scales with the frequency ω whilst the resonance field progressively shifts to lower magnetic field values as temperature decreases. A qualitatively similar behavior is observed in nanostructured samples: Figure 1(b) shows the evolution of FMR spectra for 10 nm CsNiCr NPs dispersed in PVP polymer for direct comparison with bulk behavior. Some differences with respect to the bulk behavior can be noticed at a glance by comparing spectra in Figure 1 (a) and (b), for instance, the absorption dips at low temperature result broader for NP than the bulk correspondents. These general features are also observed in X-band spectra taken by a commercial spectrometer with 3D cavity (Supporting Information).

To appreciate differences and effects of nanostructuring, we parametrize the magnetization dynamics of single domain particle in the framework of the Landau-Lifshitz-Gilbert equation [20, 21]

$$\frac{\partial \mathbf{M}}{\partial t} = \gamma_{\text{eff}}\left(\mathbf{M} \wedge \mathbf{B}_{\text{eff}}\right) + \alpha\frac{\gamma_{\text{eff}}}{M}\mathbf{M} \wedge \left(\mathbf{M} \wedge \mathbf{B}_{\text{eff}}\right), \quad (1)$$

where $\gamma_{\text{eff}} = g_{\text{eff}}\mu_B/\hbar$ is the effective gyromagnetic ratio. α is the Gilbert damping factor that can be ultimately associated to the spin-orbit coupling.[22] The effective field in each particle can be spelled out as:

$$B_{\text{eff}} = B_0 + B_{\text{MW}} + B_{\text{int}}$$

where B_0 is a static field, B_{MW} is the magnetic component of the electromagnetic field, $B_{\text{int}} = B_{\text{anis}} + B_{\text{demag}} + B_{\text{inter}}$ is the internal field which includes the anisotropy field B_{anis}, the

demagnetizing field B_{demag} and the field B_{inter} generated by inter-particle dipolar or exchange interaction by neighboring NPs.

From previous studies we expect that the magnetocrystalline anisotropy of CsNiCr NPs is related only to Ni(II) ions and it is estimated to be rather weak (0.5 kJ/m^3).[23] The surface anisotropy contribution is expected to represent the dominating term for small NPs, especially for 6 nm NPs where 40% of the atoms are located at the surface.[24] The demagnetizing field is expected to be more relevant for the smallest NPs due to their slightly elongated shape, while larger NPs have essentially cubic shape.[25] This term, however, is also affected by inter-particle dipolar interactions (B_{inter}) and thus strongly depends on the degree of dilution of the NPs in the non-magnetic matrix.[23]

The absorption dips observed in FMR spectra (Figure 1) occur when the precession of the magnetization **M** is resonant with B_{MW} at frequency ω_{res} while the line broadening is essentially given by the Gilbert damping term. For ferromagnetic systems with low anisotropy the resonance frequency of the FMR mode is expected to follow the Kittel formula,[26, 20] that, for a powder, reads

$$\omega_{res} = \gamma_{eff}(B_0 + B_{int}) = \frac{g_{eff}\mu_B}{\hbar}(B_0 + B_{int}) \qquad (2)$$

where γ_{eff} is the effective gyromagnetic ratio, $\hbar$ is the Planck constant, μ_B is the Bohr magneton.

To track the evolution of the line position as a function of the different experimental parameters, we systematically measured the FMR spectra in frequency sweep mode and, from the measured transmission (S_{21}) spectra at increasing values of B_0, we evaluated the $\partial S_{21}/\partial B_0$ derivative and extracted the resonance frequency ω_{res} (see Figure 5S in S.I.). By means of

Equation 2, the effective g-factor (g_{eff}) and the internal field $B_{int} = B_{anis} + B_{demag} + B_{inter}$ have been subsequently extracted from the linear regression of the $\omega_{res}(B_0)$ dependence. The results are plotted as a function of temperature in Figure 2(a) and 2(b). For all the samples, at 120 K i.e. in the paramagnetic phase, the effective g-factor is close to the average of the values g_{Ni} = 2.15 and g_{Cr} = 1.99 typically obtained for paramagnetic Ni(II) and Cr(III) ions. For bulk and for NP samples embedded in CTA^+, g_{eff} exhibits a maximum at $T \approx 90$ K [Figure 2(a)]. B_{int} resulted vanishingly small for $T > 90$ K while a linear increase is observed below 90 K. This reveals, once more, the transition to ferromagnetic order at T_C. Note that, the temperature dependence of g_{eff} measured for 4.8 nm NPs in CTA^+ is closer to the bulk sample than that of 8.6 nm NPs. This is in line with the outcome of SANS measurements,[19] which have clearly pointed out the presence of inter-particle interactions B_{inter}. Thus we conclude that, for NP samples in CTA^+ matrix, B_{int} is dominated by B_{inter}, while B_{demag} is the mean demagnetizing field produced by clusters of NPs.

The temperature dependence of the g_{eff} and B_{int} parameters extracted for CsNiCr 10 nm NPs diluted in PVP polymer is shown in Figure 2(b). In this case, the transition to the ferromagnetic ordered state is smoother and a downturn of g_{eff} - vs - T is observed below 60 K. This is also accompanied by a progressive increase of B_{int}, which exceeds 60 mT at 2 K. The same trend is obtained for NPs with higher dilution in PVP (see S.I.), suggesting that the temperature dependence of g_{eff} and B_{int} is not due to interparticle interactions or to macroscopic demagnetizing effects, pointing to negligible B_{inter} for PVP diluted samples. Similar behavior is observed in the temperature dependence of g_{eff} and B_{int} obtained for 6 nm and 8 nm NPs diluted in PVP [Figure 2(b)]. Worth noting is the fact that size effects are evident only at the lowest temperature on the smallest (6 nm) NPs. Also interesting to point out that, overall, $B_{int} \ll \omega_{res}/\gamma_{eff}$, while the relation $B_{int} \ll \mu_0 M_S$, where M_s = 1.47 x 10^5 A/

m is the saturation magnetization in the ordered phase, holds in the whole temperature range confirming the applicability of Equation 2 to describe the field dependence of ω_{res}[27, 28] for all bulk and nanostructured samples.

The linewidth of field-swept FMR lines (Γ_B) is usually written as [20, 29]

$$\Gamma_B = \Gamma_0 + \frac{\alpha}{2\gamma_{eff}}\omega, \qquad (3)$$

where the linear frequency dependence is related to the Gilbert damping factor (α) and Γ_0 is the zero-frequency offset, which is typically ascribed to sample inhomogeneities or to the presence of a distribution of local resonance fields across the sample.[29] To quantitatively evaluate the linewidth, we fitted the absorption dips shown in Figure 1(a, b) by means of a Lorentzian curve and extracted the half-width at half-maximum (HWHM) linewidth Γ_B. The values of Γ_B obtained for 10 nm NPs diluted in PVP are shown in Figure 2(c). In the range 100 K < T < 60 K, the frequency dependence of Γ_B gives $\alpha = 0.0010 \pm 0.0005$, while at lower temperature the slope gets steeper and we obtained $\alpha = 0.0050 \pm 0.0005$ at 5 K. The increase of Γ_B upon cooling is also caused by larger Γ_0 values. This is compatible with the upturn of the internal field shown in Figure 2(b), which may cause magnetic field inhomogeneity and broadening of the FMR line. Similar α behavior is also observed for NPs in PVP whilst a more complex temperature trend is shown by NPs in CTA^+ and by bulk samples. This is not surprising since these systems are more complex than a collection of single domain particles. Overall, the broadening of the FMR spectrum upon cooling is commonly observed in superparamagnetic NPs and typically ascribed to the progressive freezing of thermal fluctuations.[21] It is worth highlighting that the Gilbert damping coefficient $0.001 < \alpha < 0.005$ compares well with the values obtained for the lowest-order magnetostatic mode in YIG,

which amounts to 2.3 x 10^{-4} for YIG micron-sized spheres,[30] but rises up to 0.03 for YIG nanoparticles.[31]

We now turn our attention to the coupling between the FMR mode and the cavity field. To this end, we used a planar microstrip resonator (Methods) with a large filling factor and resonance frequency (ω_c = 9.51 GHz) matching the FMR mode of the CsNiCr samples in the presence of an applied magnetic field $B_{res} \approx 0.3$ T. Figure 3 shows the evolution of the transmission maps in the 2-120 K temperature range for three different CsNiCr samples: 10 nm NPs in PVP, 8.6 nm NPs in CTA^+ and bulk. NPs of 10 nm size dispersed in PVP matrix behave as a collection of independent nanomagnets as discussed in the previous section. The spectral map in Figure 3(a) shows the presence of a small absorption dip that becomes progressively broader upon cooling [Panels (b, c)]. Conversely, transmission maps taken for $T \approx T_C$ on interacting NPs of 10 nm size in CTA^+ matrix [Panels (d-f)] and on bulk samples [Panels (g-i)] show the presence of an anticrossing, with double-peak spectra that are visible for $B = B_{res}$ [Panels (k) and (l)]. The evolution of the transmission maps as a function of temperature is similar for both 10 nm NPs in CTA^+ and bulk samples as it displays, in turns, a narrow anticrossing for $T \approx T_C$, the increase of the splitting upon cooling in the temperature range between 90 and 60 K and, lastly, a progressive decrease of the transmission of the two branches at lower temperatures [Figure 3(d-i)]. The full data set with spectral maps acquired at several temperatures is reported in Supporting Information.

In the presence of a FMR mode with frequency ω_{res} given by Equation 2, the transmission of the resonator can be calculated by the input-output formula [32]

$$S_{21} = \frac{\kappa_{ext}}{i(\omega_c - \omega) + \left(\kappa_{ext} + \frac{1}{2}\kappa_{int}\right) + \frac{\Omega^2}{i(\omega_{res} - \omega) + \Gamma}} \qquad (4)$$

where Ω is the spin-photon collective coupling strength, Γ is the half-width at half-maximum (HWHM) linewidth of the FMR line in frequency units and $\kappa = \kappa_{\mathrm{int}} + \frac{\kappa_{\mathrm{ext}}}{2}$ is the total loss of the resonator given by the sum of the external (κ_{ext}) and internal (κ_{int}) contributions. The temperature dependence of the coupling strength is related to that of the magnetization $M(B_{\mathrm{res}}, T)$ of the sample by

$$\Omega = \Omega_0 \sqrt{M(B_{\mathrm{res}}, T)/M_{\mathrm{S}}}, \qquad (5)$$

where Ω_0 is a proportionality constant and M_{S} is the magnetization of saturation.[33] In the strong-coupling regime, which is characterized by $\Omega \gg (\Gamma, \kappa)$, the frequency dispersion of the two polaron branches can be reproduced by [34]

$$\omega_{\pm} = \omega_{\mathrm{c}} + \frac{\Delta}{2} \pm \frac{\sqrt{\Delta^2 + 4\Omega^2}}{2}, \qquad (6)$$

where $\Delta = g_{\mathrm{eff}} \mu_{\mathrm{B}} (B - B_{\mathrm{res}})/\hbar$.

For each temperature, we calculated the transmission maps with Equation 4 and we extracted the coupling and damping parameters that allowed us to reproduce the experimental data. The comparison between experiment and simulation is shown in Figure 3 (j-l) for the spectra taken at $B = B_{\mathrm{res}}$. The simulated transmission maps are reported in Supporting Information. The temperature dependence of Ω and Γ parameters obtained from simulations is shown in Figure 3(m) and (n), respectively. For all samples, the increase of Ω between 120 and 60 K is related to the onset of the ferromagnetic transition in this temperature (and magnetic field) range. These trends are in perfect agreement with the behavior calculated by Equation 5 (dashed line) from the magnetization data (Supporting Information). For 10 nm NPs diluted in PVP polymer, the maximum value of the coupling strength resulted in Ω (2 K) ≈ 250 MHz.

This value is much lower than those obtained for 8.6 nm NPs embedded in CTA^+ matrix and for the bulk sample, whose coupling strength exceeds 1000 MHz at low temperature. Straightforward explanation of this difference is the much larger density of spins in the latter and the presence of cooperative phenomena related to formation of clusters. The linewidth Γ follows, for the three samples, a similar temperature dependence with a progressive increase below 90 K upon cooling and values reaching 1000 MHz at 2 K. Concerning the damping rates of the microstrip resonator, the parameters extracted from simulations resulted in $16 < \kappa_{int} < 26$ MHz and $\kappa_{ext} << \kappa_{int}$, thus $\Gamma >> \kappa$. Simulations with Equation 5 evidence that such a large difference between κ and the values of Γ and Ω accounts for the weak transmission measured at low temperature for the polaron branches.

In summary, we studied the evolution of the FMR mode on bulk and nanostructured CsNiCr samples under the effects of different experimental parameters, including temperature, microwave frequency, NP size and dispersion in different non-magnetic matrices. A Gilbert damping parameter of 10^{-3} is extracted from the frequency dependence of the linewidth measured for isolated 10 nm size NPs. The coupling between CsNiCr samples and the microwave field has been investigated by means of a planar microstrip resonator. Clear differences emerge between the behavior of magnetically isolated NPs in PVP polymer and mutually interacting NPs embedded in CTA^+ matrix or the bulk sample. For 6 and 10 nm size NPs diluted in PVP polymer the condition $\Omega < \Gamma$ holds in the whole temperature range, clearly indicating the presence of weak coupling between spins and photons. Conversely, for 4.8 and 8.6 nm size NPs embedded in CTA^+ matrix, as well as for the bulk sample, the condition $\Omega > \Gamma$ holds for $T < 110$ K, evidencing the achievement of the strong coupling regime at temperature about T_C and below. With these numbers, the cooperativity, i.e. $C = \Omega/\kappa\Gamma$, results C (97 K) = 29.3 and C (4 K) = 100.2 for 8.6 nm NPs in CTA^+. Overall this

demonstrates the achievement of the strong coupling between bulk or nanostructured CsNiCr Prussian blue analogue and the cavity field of a planar resonator, which follows as a consequence of the large collective coupling that exceeds the damping of the FMR mode. These results clarify conditions for the coherent manipulation of collective spin degrees of freedom in nanostructured coordination materials and open up new possibilities for the exploitation of nanostructured coordination materials in the field of quantum magnonics and spintronics.

Methods

CsNiCr nanoparticles embedded in PVP and CTA^+ matrices were prepared following Ref. [35]: a relatively diluted aqueous solution of $K_3[Cr(CN)_6]$ (c = 1 mM/L) to an aqueous solution containing $NiCl_2,6H_2O$ (c = 1 mM/L) and 2 molar equivalents of CsCl. A light green solution is obtained. Dynamic Light Scattering (DLS) measurements performed after one hour reveals a size of 6-7 nm including the solvation shell. Scanning Transmission Electronic Microscopy (STEM) observations showed objects with a size around 5 nm. The zeta potential was measured for these particles to be $z = -31$ mV evidencing their negative charge (the counter cation being Cs^+). In order to prepare particles with larger sizes i.e. around 8 and 10 nm, the 6 nm pristine particles were used as seeds and the two precursors ($K_3[Cr(CN)_6]$ and $NiCl_2,6H_2O$) were added simultaneously to the dispersion as already described.[36] The reaction was stopped when the exact amount of precursors corresponding to the targeted size was added. The particles were recovered by two different methods: i) after one hour reaction, the organic polymer polyvinylpyrrolidone (PVP) was introduced with a [monomer]/[Ni^{2+}] ratio of 300 and then acetone was added to obtain a precipitate containing the nanoparticles coated with PVP and ii) after one hour reaction, 3 molar equivalents of cetyl trimethyl

ammonium chloride (CTACl) were added, which leads to the precipitation of the particles. It is worth noting that, here, the CTA^+ plays both the role of counter cation and organic surfactant of the negatively charged particles.

The "bulk" sample was obtained by mixing *concentrated* aqueous solutions (10 mM/L) of the two precursors, which leads to the precipitation of the micron-sized aggregates of CsNiCr as described in Ref. [15]

In all cases, X-ray powder diffraction studies showed the presence of the patterns expected for the face centered cubic structure of the particles with different sizes of 6, 8, 10 nm and larger than a micron for the "bulk" like sample.

Transmission spectroscopy data were acquired out by means of a Vector Network Analyzer in the 1-26 GHz range. These experiments were carried out in a Quantum Design PPMS by means of a home-made insert wired with two coaxial lines.[37] Broadband measurements were performed with a 500 μm wide continuous microstrip, while half-wavelength microstrip resonators were obtained by means of a 5.5 mm long metal strip separated from the feedlines by two 300 μm wide coupling gaps.[37] Planar devices were fabricated by optical lithography and wet etching in NH_4:H_2O_2 (9:1) aqueous solution of thermally evaporated Ag (3 μm)/Ti (10 nm)/sapphire (460 μm) films.

The transmission spectrum measured at 2 K and in zero applied magnetic field is shown in Supporting Information. Curve fitting of the $S_{21}(\omega)$ dependence with a conventional quasi-Lorentzian lineshape provides resonance frequency $\omega_c / 2\pi = 9.51$ GHz, loaded quality factor $Q = 635$ and insertion loss $IL = 16.2$ dB.

CsNiCr NPs and bulk samples were pressed to form a cylinder-shaped pellet (base diameter 5 mm), which were attached in the middle of the microstrip by means of a thin layer of silicone grease. The height of the sample is typically ≈ 2 mm.

Supporting Information
Supporting Information is available from the Wiley Online Library or from the author.

Acknowledgements

This work was supported from the Air Force Office of Scientific Research grant (contract no FA2386-17-1-4040).

Received: ((will be filled in by the editorial staff))
Revised: ((will be filled in by the editorial staff))
Published online: ((will be filled in by the editorial staff))

References

[1] C. W. Sandweg, Y. Kajiwara, A. V. Chumak, A. A. Serga, V. I. Vasyuchka, M. B. Jungfleisch, E. Saitoh, and B. Hillebrands**,** *Phys. Rev. Lett.* **2011**, *106*, 216601.

[2] K. Uchida, S. Takahashi, K. Harii, J. Ieda, W. Koshibae, K. Ando, S. Maekawa, and E. Saitoh, *Nature* **2008**, *455*, 778.

[3] G. E. W. Bauer, A. H. MacDonald and S. Maekawa, *Solid State Commun.* **2010**, *150*, 459.

[4] O. Rousseau, B. Rana, R. Anami, M. Yamada, K. Miura, S. Ogawa and Y. Otani, *Scie. Rep.* **2015**, *5*, 9873.

[5] A. Khitun, M. Bao and K. L Wang, *J. Phys. D: Appl. Phys.* **2010**, *43*, 264005.

[6] G. Kurizki, P. Bertet, Y. Kubo, K. Mølmer, D. Petrosyand, P. Rabl and J. Schmiedmayer, *PNAS* **2015**, *112*, 3866.

[7] D. Lachance-Quirion, Y. Tabuchi, A. Gloppe, K. Usami and Y. Nakamura, *Sci. Adv.* **2017**, *3*, e1603150.

[8] V. Cherepanov, I. Kolokolov and V. L'vov, *Phys. Rep.* **1993,** *229*, 81.

[9] A. A. Serga, A. V. Chumak and B. Hillebrands, *J. Phys. D: Appl. Phys.* **2010***, 43*, 264002.

[10] H. Liu, Chuang Zhang, H. Malissa, M. Groesbeck1, M. Kavand, R. McLaughlin, S. Jamali, J. Hao, D. Sun, R. A. Davidson, L. Wojcik, J. S. Miller, C. Boehme and Z. V. Vardeny**,** *Nature Mater.* **2018**, *17*, 308.

[11] M. Verdaguer and G. S. Girolami, in *Magnetism: Molecules to Materials V*, (Eds: by J. S. Miller and M. Drillon), Wiley-VCH, Weinheim, Germany **2005**.

[12] M. Pregelj, A. Zorko, D. Arčon, S. Margadonna, K. Prassides, H. van Tol, L. C. Brunel, and O. Ozarowski, *J. Magn. Magn. Mater.* **2007**, *316*, e680.

[13] Á. Antal, A. Jánossy, L. Forró, E. J. M. Vertelman, P. J. van Koningsbruggen, and P. H. M. van Loosdrecht, *Phys. Rev. B* **2010**, *82*, 014422.

[14] D. M. Pajerowski, J. E. Gardner, M. J. Andrus, S. Datta, A. Gomez, S. W. Kycia, S. Hill, D. R. Talham and M. W. Meisel, *Phys. Rev. B* **2010**, *82*, 214405.

[15] V. Gadet, T. Mallah, I. Castro, M. Verdaguer, P. Veillet, *J. Am. Chem. Soc.* **1992,** *114*, 9213.

[16] Y. Prado, L. Lisnard, D. Heurtaux, G. Rogez, A. Gloter, O. Stephan, N. Dia, E. Riviere, L. Catala, T. Mallah, *Chem. Commun.* **2011,** *47*, 1051.

[17] L. Catalá and T. Mallah, *Coord. Chem. Rev*. **2017**, *346*, 32.

[18] K. Ridier, B. Gillon, G. André, G. Chaboussant, L. Catala, S. Mazérat and T. Mallah, *J. Appl. Phys*. **2015**, *118*, 114304.

[19] K. Ridier, B. Gillon, G. Chaboussant, L. Catala, S. Mazérat, E. Rivière and T. Mallah, *Eur. Phys. J. B* **2017**, *90*, 77.

[20] S. V. Vonsovskii, *Ferromagnetic Resonance*, Pergamon, Oxford **1966**.

[21] J. Kliava in *Magnetic Nanoparticles*, (Ed: by S. P. Gubin), Wiley-VCH, Weinheim, Germany **2009**.

[22] M. C. Hickey and J. S. Moodera, *Phys. Rev. Lett.* **2009**, *102*, 137601.

[23] Y. Prado, S. Mazerat, E. Rivière, G. Rogez, A. Gloter, O. Stéphan, L. Catala, T. Mallah, *Adv. Funct. Mater*. **2014**, *24*, 5402.

[24] Y. Prado, M.-A. Arrio, F. Volatron, E. Otero, C. Cartier dit Moulin, P. Sainctavit, L. Catala, T. Mallah, *Chem. Eur. J.* **2013,** *19*, 6685.

[25] L. Catala, A. Gloter, O. Stephan, G. Rogez, T. Mallah, *Chem. Commun.* **2006,** 1018.

[26] C. Kittel, *Phys. Rev.*, **1948**, *73*, 155.

[27] E. Schlomann and J. R. Zeender, *J. Phys. Chem.* **1958**, *6*, 257.

[28] R. S. de Biasi and T. C. Devezas, *J. Appl. Phys*. **1978**, *49*, 2466.

[29] A. Barman and J. Sinha, *Spin Dynamics and Damping in Ferromagnetic Thin Films and Nanostructures*, Springer, Cham, Switzerland, **2018**.

[30] a) H. Huebl, C. W. Zollitsch, J. Lotze, F. Hocke, M. Greifenstein, A. Marx, R. Gross and S. T. B. Goennenwein, *Phys. Rev. Lett.* **2013**, *111*, 127003; b) Y. Tabuchi, S. Ishino, T. Ishikawa, R. Yamazaki, K. Usami and Y. Nakamura, *Phys. Rev. Lett.* **2014**, *113*, 083603; c) X. Zhang, C.-L. Zou, L. Jiang and H. X. Tang, *Phys. Rev. Lett.* **2014**, *113*, 156401; d) X. Zhang, C.-L. Zou, N. Zhu, F. Marquardt, L. Jiang and H. X. Tang, *Nat. Commun.* **2015**, *6*, 8914; e) X. Zhang, C.-L. Zou, L. Jiang and H. X. Tang, *Sci. Adv.* **2016**, *2*, e1501286; f) N. Kostylev, M. Goryachev and M. E. Tobar, *Appl. Phys. Lett.* **2016**, *108*, 062402*;* g) R. G. E. Morris, A. F. van Loo, S. Kosen and A. D. Karenowska**,** *Sci. Rep.* **2017**, *7*, 11511.

[31] V. Sharma, J. Saha, S. Patnaik, B. K. Kuanr, *J. Magn. Magn. Mater.* **2017**, *439*, 277.

[32] C. Bonizzoni, A. Ghirri, M. Atzori, L. Sorace, R. Sessoli and M. Affronte, *Sci. Rep.* **2017**, 7, 13096.

[33] A. Ghirri, C. Bonizzoni, F. Troiani, N. Buccheri, L. Beverina, A. Cassinese and M. Affronte, *Phys. Rev. A* **2016**, *93*, 063855.

[34] A. Ghirri, C. Bonizzoni, D. Gerace, S. Sanna, A. Cassinese and M. Affronte, *Appl. Phys. Lett.* **2015**, *106*, 184101.

[35] D. Brinzei, L. Catala, N. Louvain, G. Rogez, O. Stéphan, A. Gloter and T. Mallah**,** *J. Mater. Chem.* **2006**, *16*, 2593–2599.

[36] L. Catala, D. Brinzei, Y. Prado, A. Gloter, O. Stéphan, G. Rogez, and T. Mallah, *Angew. Chem. Int. Ed*. **2009**, *48*, 183.

[37] A. Ghirri, C. Bonizzoni, M. Righi, F. Fedele, G. Timco, R, Winpenny and M. Affronte, *Appl. Mag. Reson.* **2015**, *46*, 749.

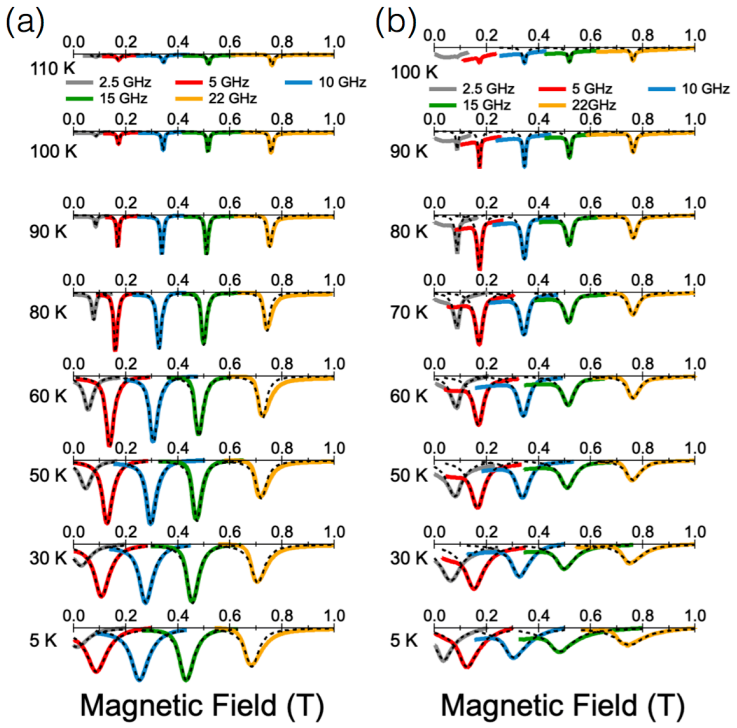

Figure 1. Transmission spectra measured at different frequency and temperature for (a) bulk CsNiCr and (b) 10 nm NPs dispersed in PVP polymer. Dashed lines show the fit with a Lorentzian lineshape.

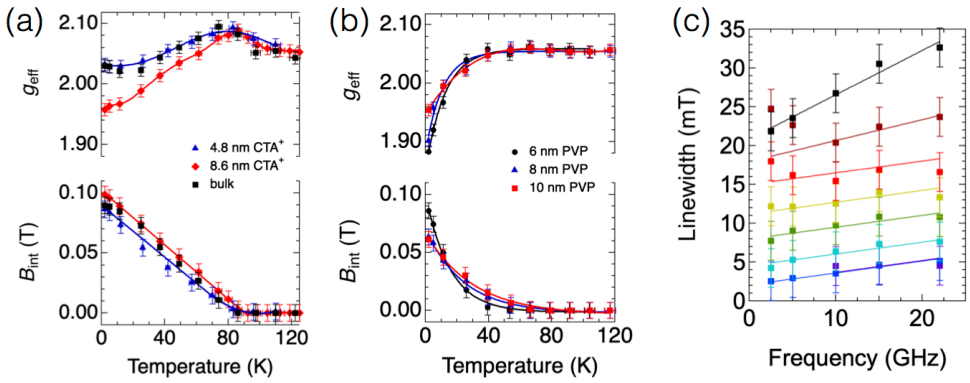

Figure 2. (a, b) Temperature dependence of the effective *g*-factor and internal field as function of temperature. Lines are guides for the eyes. (c) Frequency dependence of the HWHM linewidth extracted for 10 nm NPs in PVP. Solid lines display the trends obtained with Equation 3.

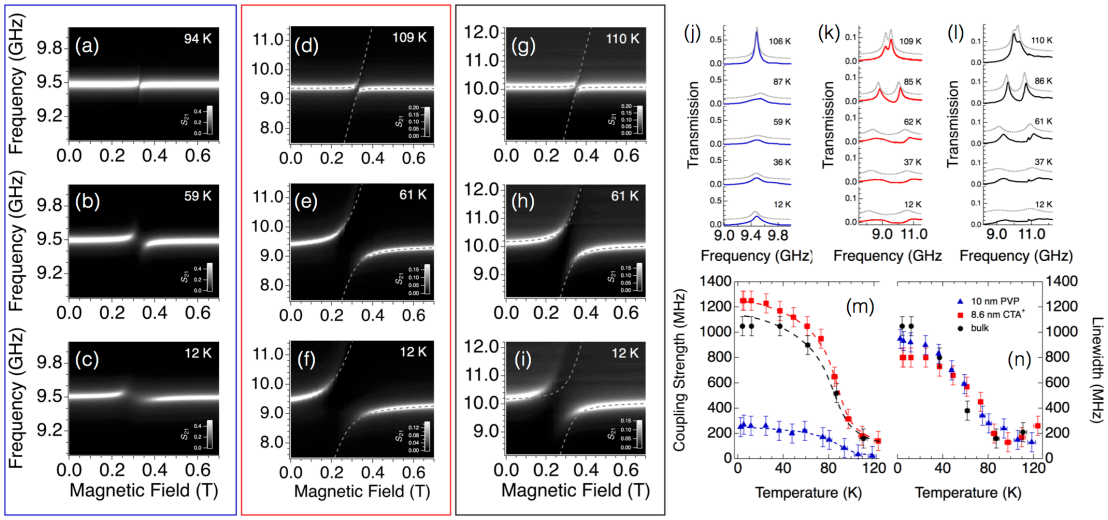

Figure 3. Transmission maps obtained at different temperature for (a, b, c) 10 nm NPs in PVP; (d, e, f) 8.6 nm NPs in CTA+; (g, h, i) bulk sample. Dashed lines show the calculated frequency dependence of the polariton branches. For each temperature, data are normalized to the maximum transmission. (j, k, l) Transmission spectra taken at the resonance field respectively for 10 nm NPs in PVP, 8.6 nm NPs in CTA^+ and bulk. Dashed lines show the spectra calculated from the input-output formula. For each sample and temperature, the line position is calculated with the effective *g*-factor and internal field parameters obtained from the FMR characterization. (m, n) Temperature dependence of the extracted values of collective coupling strength and HWHM linewidth.

Ferromagnetic resonance studies on bulk and nanostructured CsNiCr Prussian blue analogue are carried out in a wide temperature range across the Curie temperature at 90 K. A Gilbert damping parameter of 10^{-3} is extracted from the frequency dependence of the linewidth of 10 nm size isolated nanoparticles. The large collective spin-photon coupling obtained for bulk and interacting nanoparticles in a planar microstrip resonator allows for the achievement of the strong coupling regime.

Ferromagnetic resonance, Coherent spin-photon coupling, Magnonics, Prussian Blue Analogues, Coordination nanoparticles

A. Ghirri*, C. Herrero, S. Mazérat, T. Mallah, O. Moze and M. Affronte

Coupling nanostructured CsNiCr Prussian Blue Analogue to resonant microwave fields

ToC figure

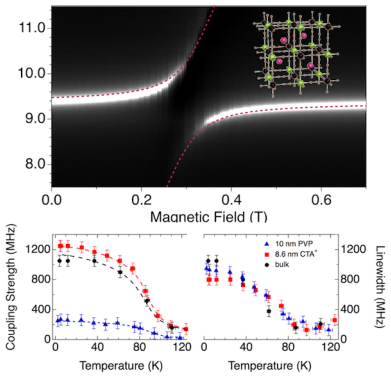

Supporting Information

Coupling nanostructured CsNiCr Prussian Blue Analogue to resonant microwave fields

Alberto Ghirri, Christian Herrero, Sandra Mazérat, Talal Mallah, Oscar Moze and Marco Affronte*

1. FMR spectra in 3D cavity

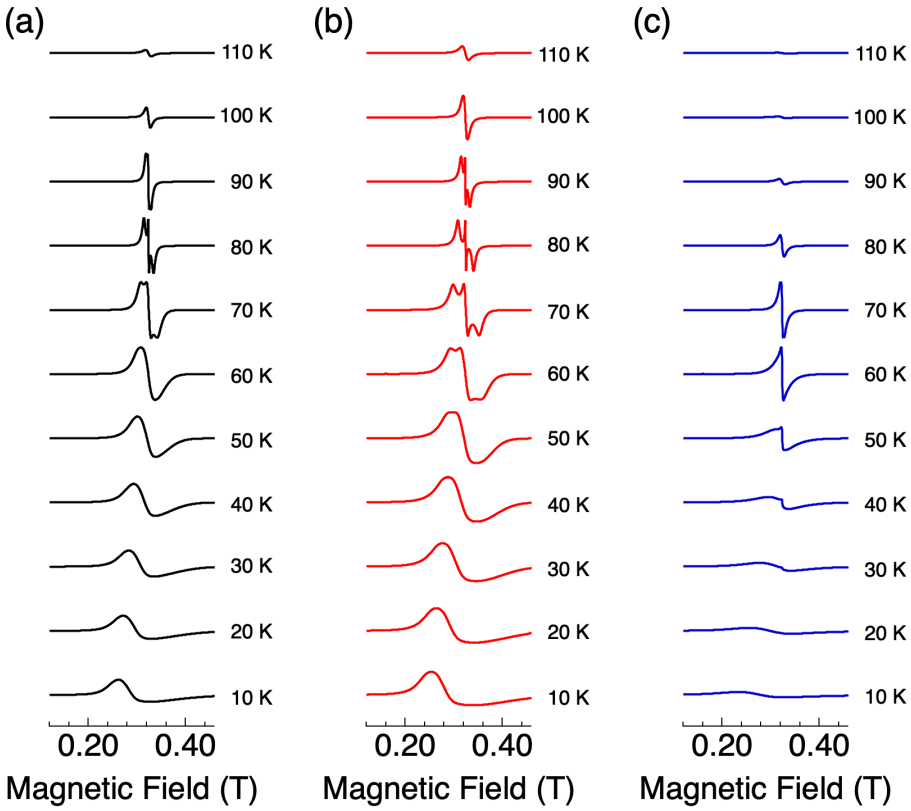

Figure S1. Field-swept derivative FMR spectra taken at 9.38 GHz. (a) 10 nm NPs diluted in PVP. (b) 10 nm NPs highly diluted in PVP. (c) 6 nm NPs highly diluted in PVP.

FMR spectra were acquired using a Bruker ELEXSYS 500 spectrometer equipped with a Bruker ER 4119HS X band resonator, an Oxford Instrument continuous flow ESR 900 cryostat, and an Oxford ITC 503 temperature control system under the following experimental conditions: 9.38 GHz microwave frequency, 0.250 mW microwave power, 14

dB gain, 10 Gauss modulation amplitude, 100 kHz modulation frequency and a sampling time of 163 ms.

FMR spectra taken on 10 nm size NPs diluted in PVP polymer are shown in Figure S1(a). Similarly to the FMR data reported in the main text, a faint first-derivative FMR peak is already visible at 110 K, whose intensity progressively increases upon cooling to reach the maximum value at about 70 K. Below 60 K the intensity gradually decreases and the line broadens out. This is also accompanied by a progressive shift of the resonance towards lower magnetic fields. While similar trends were observed for 10 nm size NP samples with higher dilution, larger broadening emerges for 6 nm size NPs [Figure S1(b,c)]. Indeed, considering that for both 6 nm and 10 nm NPs the intensity of the FMR line increases upon cooling in a similar fashion (Figure S2), for highly diluted 10 nm size NPs the ratio between the peak-to-peak amplitude at 10 K and 70 K is 0.63, while for 6 nm NPs with comparable dilution the same ratio is just 0.09. This behavior is good agreement with the trends evidenced by FMR studies reported in the main text.

An additional narrow FMR component with *g*-factor ≈ 2 appears in the temperature range between 90 and 60 K, for 10 nm NPs, and between 50 and 30 K, for 6 nm NPs. The appearance of a sharp FMR line at intermediated temperature has been already reported for diluted superparamagnetic nanoparticles.[1] A possible explanation for this effect is the cancellation, at sufficiently high temperature, of the anisotropy-related broadening for particular thermally activated excited states.[1]

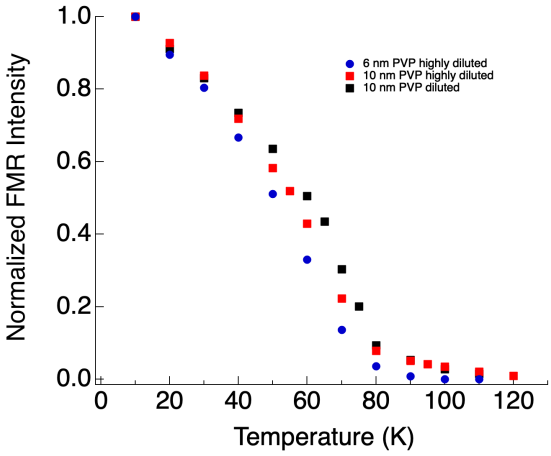

Figure S2. Temperature dependence of the intensity obtained from double integration of the derivative FMR spectra. Each curve is normalized to the value at 10 K.

2. Characterization of the microstrip resonator

The transmission spectrum of the Ag/sapphire microstrip resonator measured at 2 K in zero applied field is shown in Figure S4. This spectrum is acquired with an incident power of -13 dBm. The attenuation of the coaxial lines has been taken into account and removed.

The lineshape can be reproduced by a quasi-Lorentzian lineshape[2]

$$S_{21} = \frac{10^{-\frac{IL}{20}}}{\sqrt{1 + Q_L^2\left(\frac{\nu}{\nu_C} - \frac{\nu_C}{\nu}\right)^2}}$$

where $\nu_C = \omega_C/2\pi$, IL is the insertion loss and Q_L is the (loaded) quality factor. The best fit of the experimental data at 2 K provides ν_c = 9.51 GHz, Q = 635 and IL = 16.2 dB.

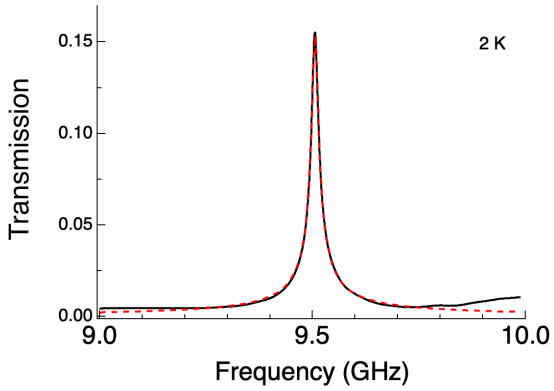

Figure S4. Transmission spectrum of the microstrip resonator in zero applied magnetic field (T = 2 K). A pellet of 10 nm CsNiCr NPs diluted in PVP was installed on the resonator. The dashed line displays the fit with a conventional a quasi-Lorentzian lineshape.

3. Frequency-swept FMR spectra of bulk and nanostructured CsNiCr samples

In order to study the evolution of the FMR mode across the ferromagnetic transition and below, we measured, at several temperatures, the transmission of a broadband microstrip transmission line with a CsNiCr sample positioned in the middle of the microstrip. The transmission spectra were measured as a function of frequency for increasing values of the applied magnetic field. We then calculated the derivative of the transmission with respect to the magnetic field in order to enhance the visibility of FMR line over the non-magnetic background of the microstrip.

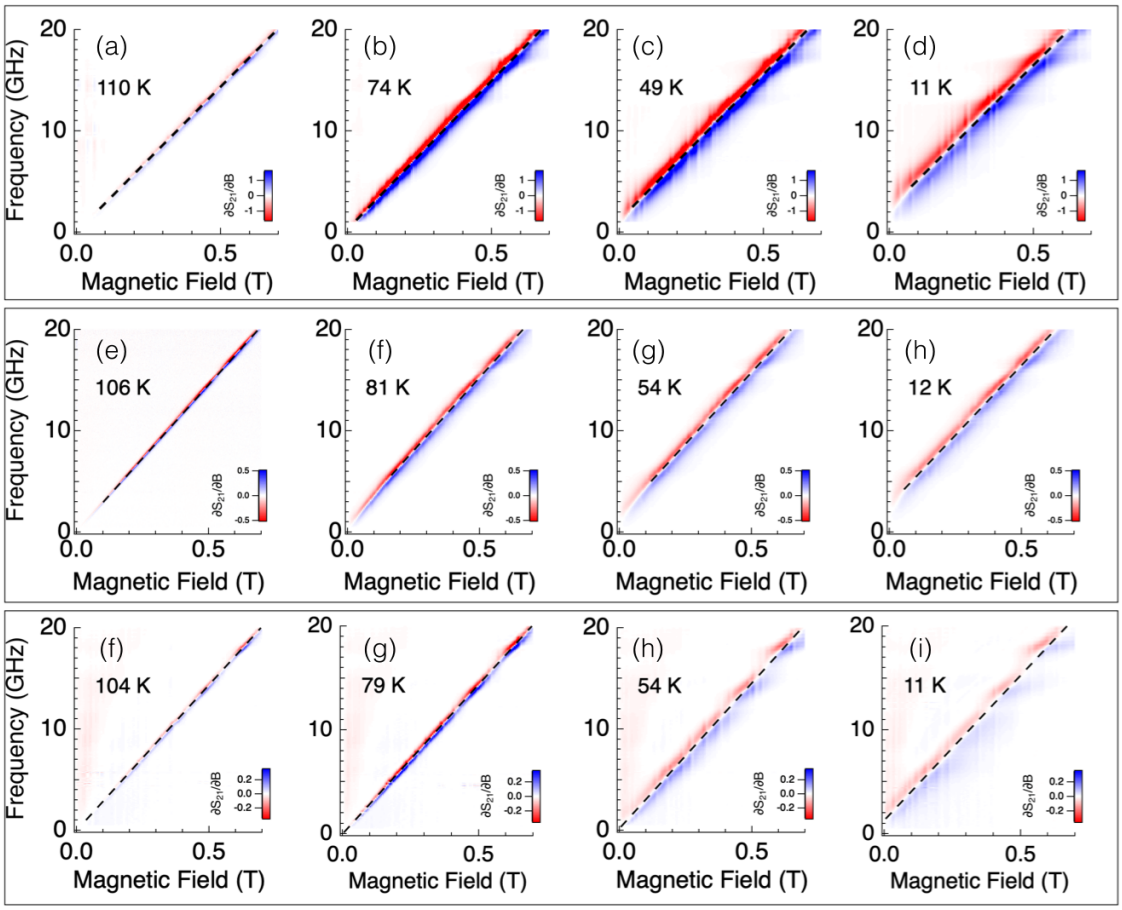

Figure S5. Spectral maps showing the derivative of the transmission with respect to the magnetic field. (a-d) Bulk sample of CsNiCr. (e-h) 8.6 nm NPs CTA^+ matrix. (f-i) 10 nm NPs in PVP polymer. Dashed lines show the linear regression with Equation 2 of the communication.

Figure S5 shows some representative spectral maps measured at different temperatures for the bulk CsNiCr sample, for 8.6 nm NPs embedded in CTA^+ matrix and 10 nm NPs dispersed in

PVP polymer. The resonance frequency has been extracted by considering, for each field, the zero-crossing frequency of the spectrum. For all samples, a FMR mode with resonance frequency proportional to the applied magnetic field is clearly visible. At temperature $T > 90$ K, the FMR line is faint while its amplitude increases in proximity of the ferromagnetic transition. At low temperature, the FMR mode becomes progressively broader.

Figure S5 evidences differences between bulk and nanostructured samples in different non-magnetic matrices. The bulk sample, being more concentrated, provides the highest amplitude of the FMR derivative peak, while the PVP sample provides the lowest amplitude, being the less concentrated. We have used Equation 2 to fit the linear dependence of the resonance frequency from the applied magnetic field. The linear fits are shown by dashed lines in Figure S5. In particular, we note that bulk and 8.6 nm NPs in CTA^+ show, at each temperature, a comparable intercept, which is larger than what is obtained for 10 nm NPs in PVP.

4. Additional FMR results

Figure S6 shows the comparison between the parameters extracted for 10 nm NPs with different degree of dilution in PVP polymer. The g_{eff} and B_{int} parameters obtained from such samples are in very good agreement, confirming that these values are not related to the presence of inter-particle interactions.

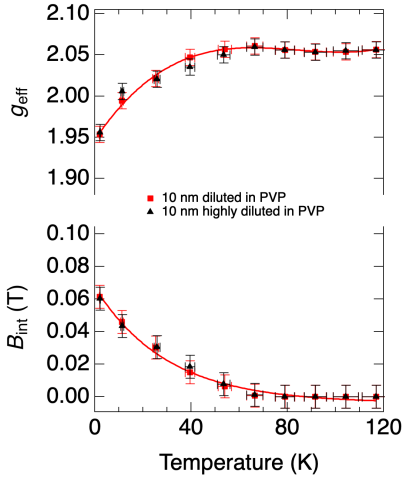

Figure S6. Comparison between the parameters extracted for 10 nm NPs with different degree of dilution in PVP polymer. Lines are guides for the eye.

5. Magnetization measurements

The evolution of the magnetization as a function of temperature is shown in Figure S6. Data are taken with an applied magnetic field of 0.3 T. For 10 nm PVP and 8.6 nm CTA^+ NPs, an increase of the magnetization is observed upon cooling below 90 K. For 6 nm NPs the magnetization start to increase at lower temperature.

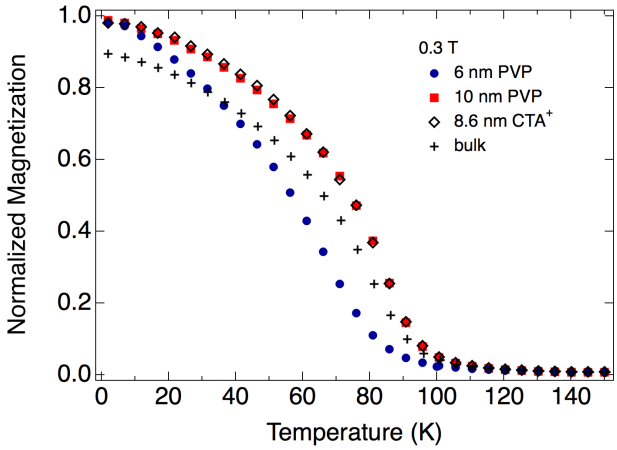

Figure S7. Normalized magnetization measured on 6 nm and 10 nm NPs diluted in PVP and on 8.6 nm NPs embedded in CTA^+. The applied magnetic field is 0.3 T. Data are normalized to the saturation value measured for each sample at T = 2 K and B = 7 T.

6. Additional transmission spectroscopy results

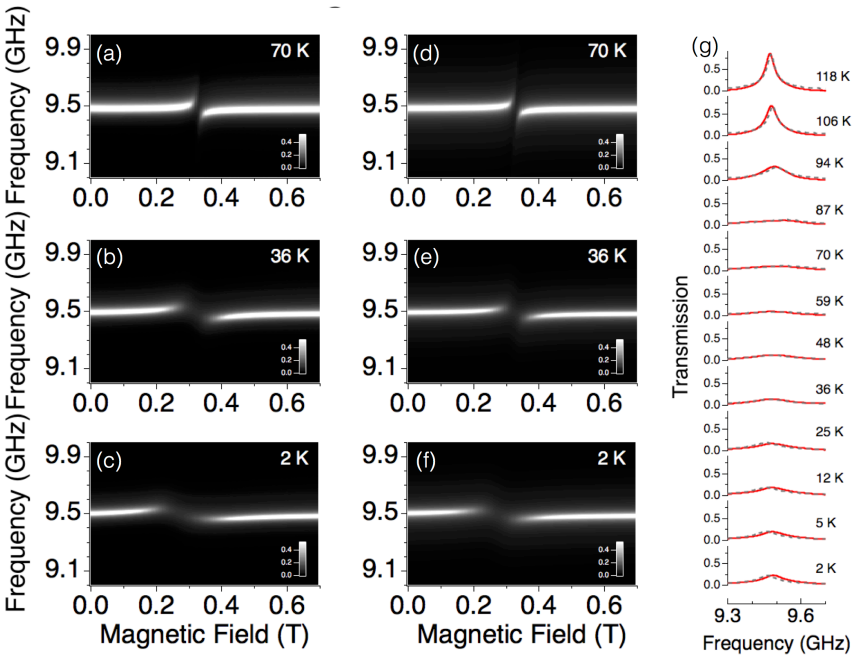

Figure S8. Transmission maps measured on 10 nm NPs diluted in PVP matrix. (a, b, c) Transmission spectral maps measured at different temperatures and (d, e, f) comparison with input-output simulations. (g) Evolution of the on resonance spectra for several temperatures. Dashed lines show the simulated spectra.

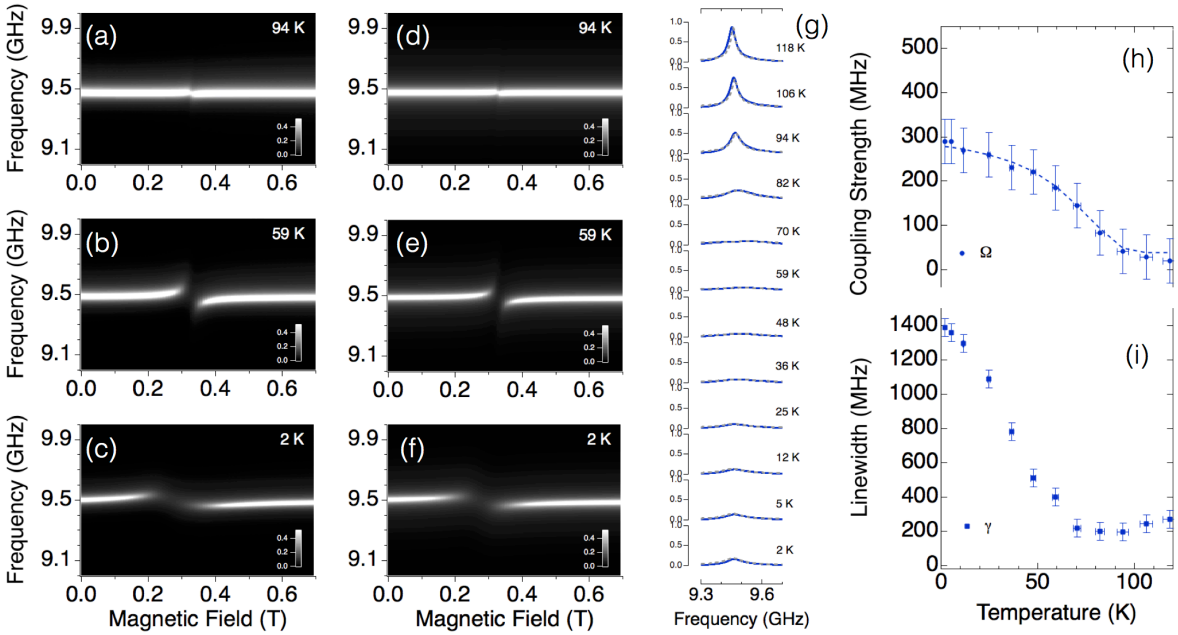

Figure S9. Transmission maps measured on 6 nm NPs diluted in PVP matrix. (a, b, c) Transmission spectral maps measured at different temperatures and (d, e, f) comparison with

input-output simulations. (g) Evolution of the on resonance spectra for several temperatures. Dashed lines show the simulated spectra. (h, i) Temperature dependence of the extracted collective coupling strength and HWHM linewidth.

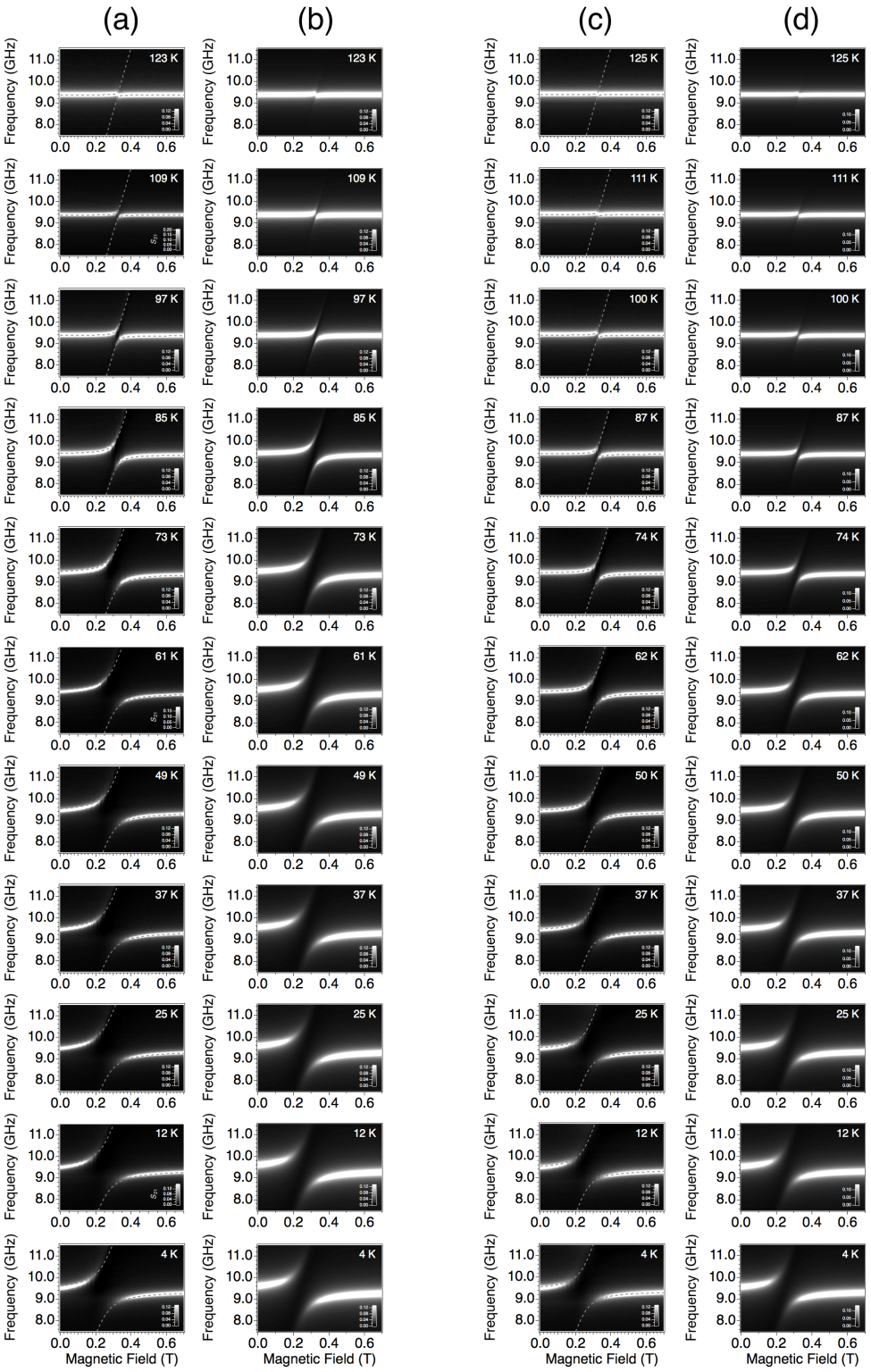

Figure S10. Temperature evolution of the transmission spectral maps measured for CsNiCr NPs embedded in CTA^+ matrix. The samples have comparable size. Column (a) displays 8.6 nm NPs and column (b) input-output simulations. Column (c) displays 4.8 nm NPs and

column (d) input-output simulations. Dashed lines display the calculated frequency dispersion of polaron branches.

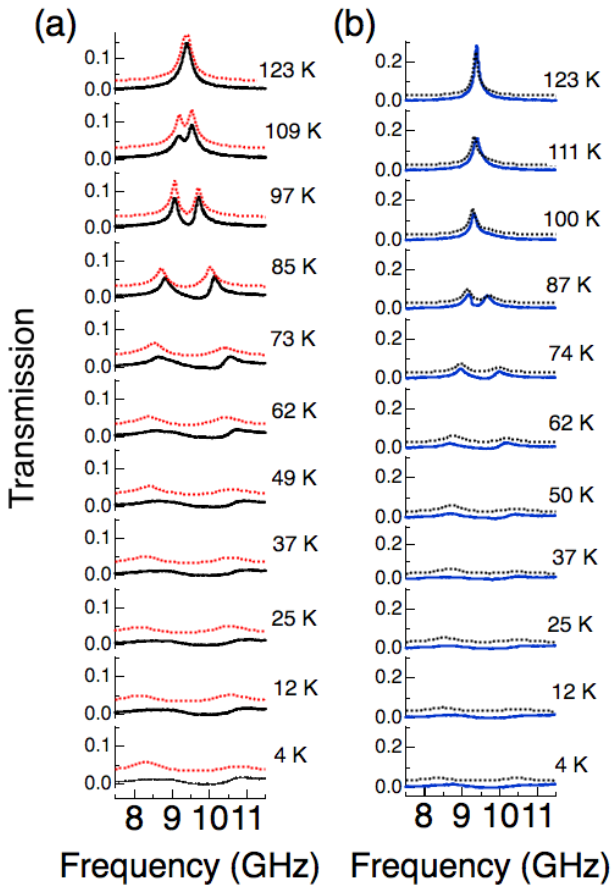

Figure S11. Temperature evolution of the transmission spectra measured at the resonance field for (a) 8.6 nm NPs in CTA^+ and (b) 4.8 nm NPs in CTA^+. Dashed lines show spectra calculated by input-output formula.

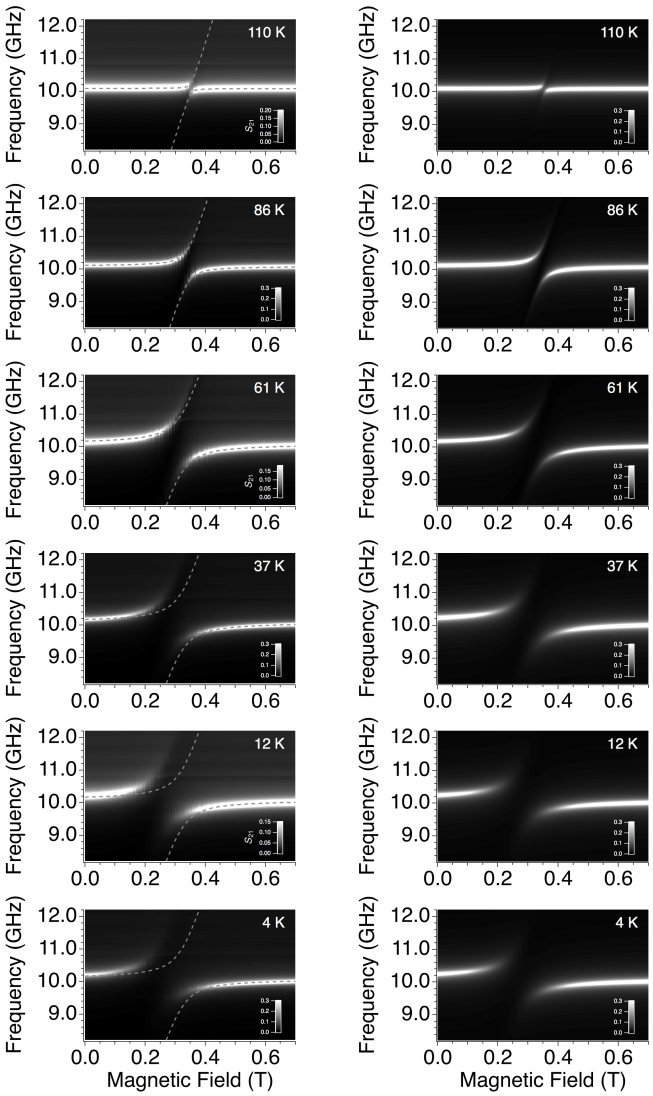

Figure S12. Temperature evolution of the transmission spectral maps measured for a bulk CsNiCr sample. (left) Experimental data. (right) Input-output simulation.

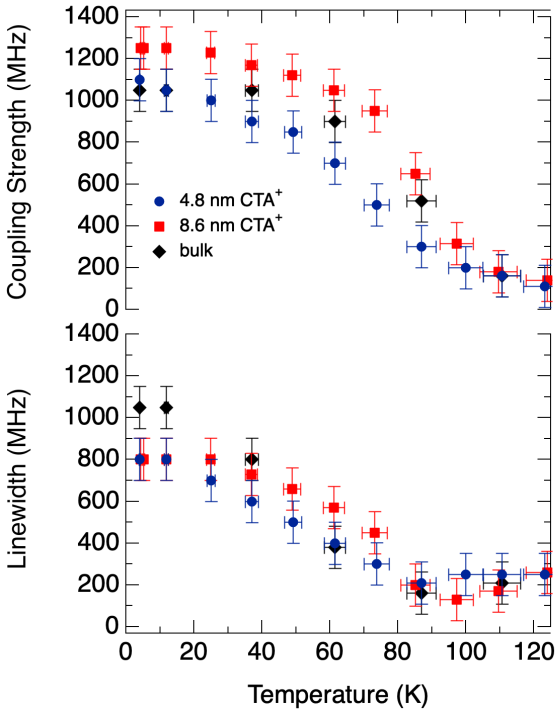

Figure S13. Temperature dependence of coupling strength and linewidth parameters extracted for 8.6 nm and 4.8 nm CsNiCr NPs diluted in CTA^+ and the bulk sample.

References

[1] N. Noginova, F. Chen, T. Weaver, E. P. Giannelis, A. B. Bourlinos and V. A. Atsarkin, *J. Phys.: Condens. Matter.*, **2007**, *19*, 246208.

[2] A. Ghirri, C. Bonizzoni, D. Gerace, S. Sanna, A. Cassinese and M. Affronte, *Appl. Phys. Lett.*, **2015**, *106*, 184101.